Improved Zone 1 Top-line Tilting Scheme for Polygonal Distance Protection in the Outgoing Line of Type-4 Wind Parks

Ma, Kaiqi; Høidalen, Hans Kristian ; Chen, Zhe; Bak, Claus Leth

Published in:
CSEE Journal of Power and Energy Systems

DOI (link to publication from Publisher):
10.17775/CSEEJPES.2021.07870

Publication date:
2023

Document Version
Publisher's PDF, also known as Version of record

Improved Zone 1 Top-line Tilting Scheme for Polygonal Distance Protection in the Outgoing Line of Type-4 Wind Parks

Kaiqi Ma, Hans Kristian Høidalen, *Senior Member*, *IEEE*, Zhe Chen, *Fellow*, *IEEE*, and Claus Leth Bak, *Senior Member*, *IEEE*

***Abstract*—The impedance element in distance protection equipment in the outgoing line of a wind park (WP) may be heavily affected by the fault response of the WP. During resistive grid faults, relay over-reach (or under-reach) may manifest, depending on the fault current regulating requirements in the specific grid code deployed in WP and the fault conditions. Aiming at potential solution, i.e. the existing zone 1 (fast tripping zone, non-delayed) top-line tilting (Z-1-TLT) function in modern numerical relays, this paper first assesses its adaptability under the WP integrated background. Combining the principle of Z-1-TLT itself and fault modeling to the WP, an improved Z-1-TLT scheme is developed, which can actively compensate for the possible relay overreach or under-reach during resistive faults, utilizing relay side fault quantities only. Aiming at the needless action of the new Z-1-TLT scheme against certain faults, malfunction risk area detection and dead zone detection are introduced as auxiliary criteria to optimize protective efficiency. Simulation results prove the improved Z-1-TLT scheme can effectively improve reliability of distance protection deployed in the WP outgoing line.**

***Index Terms*—Distance protection, fault current regulating requirement, grid code, relay over-reach (under-reach), wind park, zone 1 top-line tilting.**

I. Introduction

In decades, renewable energies were vigorously developed to substitute for fossil energy resources. This is especially evident in a conventional resource-constrained region, e.g. Denmark, where wind power is most prominent [1]. At present, WPs with large (or medium) capacities are popular generation systems in electrical industry [2]. Many countries have published grid codes for WPs, among which, in the event of grid faults, the requirement of fault-ride-through specifies WPs to remain connected through faults on the power system [3]. However, the different fault responses of WPs compared to the synchronous generators (SGs), e.g. the smaller short-circuit capacity, the harmonics, and the susceptibility to fault controls, bring in adaptability issues for network protections [2], [4].

Distance protection is a widely used line protection scheme. For its application in a WP-connected system, many research works have reported adaptability issues. References [5]–[7] have pointed out that frequency deviation of the fault current produced by the type-3 (Doubly-fed induction generator wind turbines based) WPs may affect transient performance of the impedance element. For this, time-domain distance protections can handle such transient issues due to time domain data based distance measuring mechanism [7], [8].

In contrast, distance protection is more problematic in a system connecting type-4 (Full-converter wind turbines based) WPs. To date, different malfunction risks of distance protection, e.g. impedance element [9], [10], directional element and relay characteristic [11], as well as phase selector [12], have been reported. Specific to the impedance element, the main risk is the reactance measuring error-caused relay overreach or under-reach during resistive faults, which has drawn substantial attention. Considering the fully controllable fault behaviors of type-4 WPs, the control-based solutions have been proven effective to improve reactance measuring accuracy of the impedance element [13], [14]. Generally, they need a certain modification for the current regulating requirements (in grid codes) under fault conditions, especially the active component of positive sequence current. In the aspect of protection improvements, reference [9] revises the traditional distance protection by incorporating a zero-sequence impedance-based complementary criterion. However, it is not workable for non-grounded faults. In addition, adaptive distance protections accounting for the control characteristics of type-4 WPs or -like generating plants are promising and have gotten lots of attention. In [15], the adaptive tripping boundary set method for the quadrilateral relay is reported, where the WP is seen as a Thevenin circuit and the equivalent source impedance in positive and negative sequence circuits are deemed to be the same. This does not conform with the controlled model characteristics of realistic type-4 WPs. In [16], [17], two distance protection solutions, working for the estimation of accurate line impedance up to fault point, are developed to eliminate the measured 'virtual' impedance during resistive faults. However, they apply to a transmission network in homogeneity only.

Manuscript received October 22, 2021; revised May 20, 2022; accepted June 12, 2022. Date of online publication August 18, 2022; date of current version September 5, 2022. This work was supported by the EUDP Project 'Voltage Control and Protection for a Grid towards 100% Power Electronics and Cable Network (COPE)' (EUDP17-I: 12561).

K. Q. Ma (corresponding author, e-mail: kma@energy.aau.dk), C. L. Bak and Z. Chen are with the Department of Energy, Aalborg University, 9220 Aalborg, Denmark.

H. K. Høidalen is with the Department of Electric Power Engineering, Norwegian University of Science and Technology, NO-7491, Trondheim, Norway.

DOI: 10.17775/CSEEJPES.2021.07870

Under such conditions, the current distribution coefficient(s) is (are) properly simplified. So does the alterable Mho relay based on an adaptive setting impedance in [18]. Besides, the deployment of balanced current control in grid side converters (GSCs) is mainly considered in [18]. Recent advancements on the technical rule of reactive current in the negative sequence system has been reported for GSC-based power plants [19]. But the active power exchange in a negative sequence system is undesired [20], this may conflict with the negative sequence impedance shaping scheme in [17]. In addition, [21] provides an new distance relaying method to overcome the relay under -reach issue in a multi-terminal system connecting converter -interfaced power sources. However, auxiliary communication is needed to obtain the information at remote terminals.

Actually, some modern numerical (polygonal) relays, e.g. Siemens 7SA6, 7SA522, etc., have the function of tilting the zone 1 top-line to avoid the possible overreach problem for the application at the power sending end in SG-dominated grids [22]. However, it is problematic to deal with the complex risks in the outgoing line of a WP, which can be either overreach or under-reach. This paper aims at improving the existing Z-1-TLT scheme to a good fit in the outgoing line of the type-4 WP. The improved Z-1-TLT scheme, compatible with typical regulating requirements of WP's fault current specified in grid codes, can compensate for unexpected 'virtual' reactance measurements during resistive grid faults. Coordinating with the auxiliary criteria of malfunction risk area and dead zone detections, the new scheme avoids superfluous or unreliable operations during certain faults, which enhances its reliability and efficiency.

The rest of this paper is organized as follows. In section 2, the protective problem of the existing Z-1-TLT scheme is analyzed based on the control compatible fault modeling of WPs. Furthermore, the improved Z-1-TLT scheme is deduced in section 3; Section 4 organizes the simulation verification and influence analysis; discussion and concluding remarks are outlined in sections 5 and 6, respectively.

II. Protective Issue Analysis

A. Existing Z-1-TLT Scheme in Polygonal Distance Relay

Figure 1 shows the single-line diagram of a WP-connected transmission system. Z, $Z_{\rm r}$ and, $Z_{\rm s}$ represent the impedance of the line, the main grid, and the WP side system, respectively. $\dot{\boldsymbol{I}}_{\rm s,r}$ and $\dot{\boldsymbol{U}}_{\rm s,r}$ are, respectively, the current and voltage phasors at terminals S and R. F is the fault position. $\dot{\boldsymbol{I}}_{\rm f}, R_{\rm f}$, and m are the fault current, the fault resistance, and the per unit fault distance. DR denotes the distance relay.

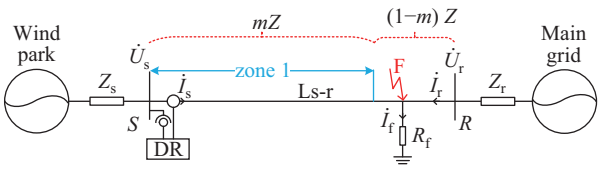

Fig. 1. Single-line diagram of the fault network connecting type-4 WP.

The apparent impedance of relay DR meets,

$$Z_{\rm app} = mZ + \left(1 + \frac{\dot{\boldsymbol{I}}_{\rm r}}{\dot{\boldsymbol{I}}_{\rm s}}\right) R_{\rm f} = mZ + \Delta Z \tag{1}$$

In (1), the modulating impedance ΔZ will include a negative contribution if the currents are out of phase, referring to the analysis in the case of an SG-dominated power grid [22]. For this impact, the existing Z-1-TLT scheme in the modern numerical relays has been proven effective, which is an off-line method [22]. In detail, one needs to find a suitable tilting angle for the zone 1 top-line in advance so that over-reach is avoided at the sending terminal. In principle, the tilting angle is estimated from the modulating impedance under the assumption of a remote terminal fault. Reference [15] deduced the universal expression of ΔZ, being a function of variables m and $R_{\rm f}$. For a forward fault AG, the modulating impedance is written as,

$$\Delta Z = \frac{3R_{\rm f}}{D_{\rm D} + 2D_1 + D_0(1+3k_0)} \tag{2}$$

$$D_1 = \frac{(1-m)Z_1 + Z_{\rm r1}}{Z_{\rm s1} + Z_1 + Z_{\rm r1}},\ D_0 = \frac{(1-m)Z_0 + Z_{\rm r0}}{Z_{\rm s0} + Z_0 + Z_{\rm r0}} \tag{3}$$

where $k_0 = (Z_0 - Z_1)/Z_1$ is the zero sequence compensation factor. Subscripts "1, 2, 0" denote the positive, negative, and zero sequence components in this paper. D_1 and D_0 are the current distribution factors in positive and zero sequence systems, respectively. $D_{\rm D}$ is another factor related to the variables m and $R_{\rm f}$, the pre-fault power transfer angle ϑ, the voltage amplitude ratio ρ, and system impedance parameters.

$$D_{\rm D} = \frac{\left(1 - \rho e^{-{\rm j}\vartheta}\right)(3R_{\rm f} + Z_{\rm sum})}{(Z_{\rm s1} + mZ_1)\left(\rho e^{-{\rm j}\vartheta}\right) + (1-m)\,Z_1 + Z_{\rm r1}} \tag{4}$$

where $Z_{\rm sum}$ represents the sum of positive, negative, and zero sequence impedance of the network in Fig. 1.

If set $m = 1$ (i.e. a remote terminal fault) and ignore the voltage amplitude ratio (i.e. $\rho = 1$), ΔZ is the same as in [22]. The expected tilting angle is written as,

$$\theta_{\rm AMI} = \angle\left(\Delta Z|_{m=1}\right) \tag{5}$$

One needs the maximum $R_{\rm f}$ to be covered and at least two or three intermediate values to adapt the existing Z-1-TLT, see [22] in detail.

B. Problem Statement

The above formulation relies on a fixed source impedance $Z_{\rm s}$, equal in positive and negative sequence circuits, and is problematic for a source of type-4 WP.

As reported in [20], a type-4 WP can be seen as a voltage (at the point of common coupling (PCC)) controlled current source when it follows with a specific grid code. Under such conditions, the fault behavior of type-4 WPs is fully controlled by the GSC. Take the popular decoupled sequence control (DSC) scheme of the GSC given in the WP aggregating model of Fig. 2(a), for example. The steady-state currents in the sequence component systems during unbalanced grid faults can be expressed as,

$$\begin{cases} \dot{\boldsymbol{I}}_1 = \left(I''_{d1} + {\rm j}I''_{q1}\right)\exp\left({\rm j}\angle\left(\dot{\boldsymbol{V}}_1\right)\right) \\ \dot{\boldsymbol{I}}_2 = \left(I''_{d2} + {\rm j}I''_{q2}\right)\exp\left({\rm j}\angle\left(\dot{\boldsymbol{V}}_2\right)\right) \end{cases} \tag{6}$$

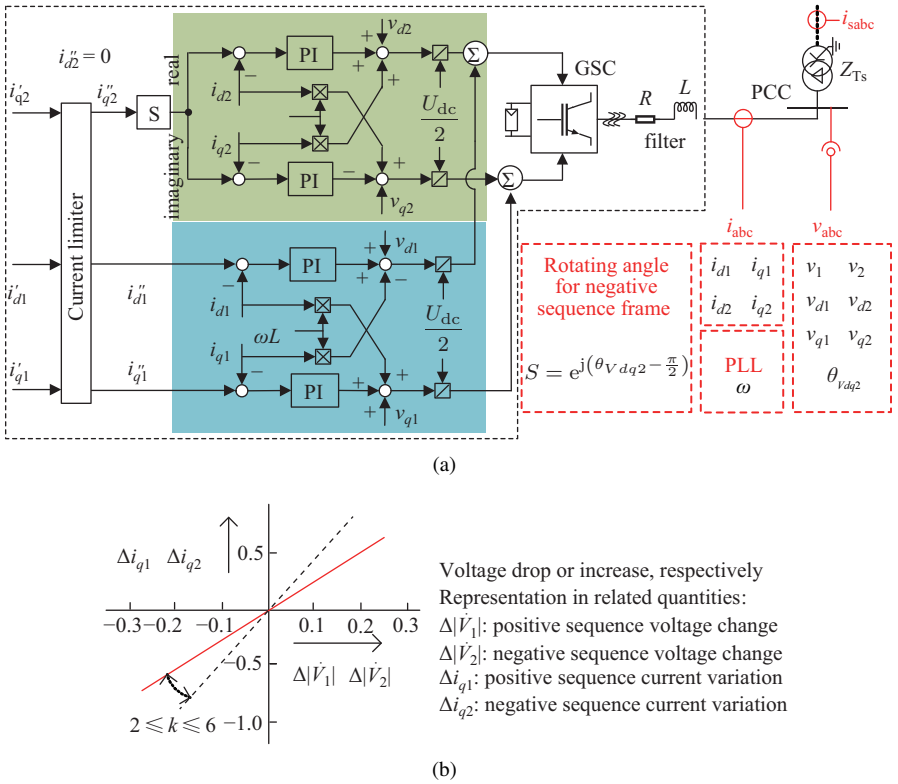

Fig. 2. Typical fault control of the GSC. (a) Diagram of DSC scheme (b) Advanced reactive current regulation requirement [19].

where the current and voltage phasors $\dot{\boldsymbol{I}}$ and $\dot{\boldsymbol{V}}$, and the current commands I''_{dq} in the dq reference frame correspond to the time-domain quantities (in lower-case format) of Fig. 2.

During normal system operation, the WP mainly produces active power. After grid faults, some transmission system operators (TSOs), e.g. in Ireland, encourages continuing active power generation [23]. In contrast, some other TSOs, e.g. in Denmark and German, require prior reactive power supports of WPs, however, active power generation within the secure capacity of WP is still desired for economic reasons [23].

According to the recent German technical rule of reactive current regulation, as displayed in Fig. 2(b), the initial current commands I'_{dq} can be defined. Furthermore, I'_{dq} can be revised based on the GSC current limits $I_{\rm lim}$ and $I_{q\rm lim}$ in the phasor domain and q-axis, as given in (7)–(8),

$$\begin{cases} I''_{q1} = \dfrac{I'_{q1}}{M} = \dfrac{-K_1(1-|\dot{\boldsymbol{V}}_1|)}{M} \\ I''_{q2} = \dfrac{I'_{q2}}{M} = \dfrac{K_2|\dot{\boldsymbol{V}}_2|}{M} \end{cases}, M = \max\left(1, \frac{|I'_{q1}| + |I'_{q2}|}{I_{q\rm lim}}\right) \tag{7}$$

$$\begin{cases} I''_{d1} = \min\left(I'_{d1} = \frac{P_{\rm in}}{v_{d1}}, \sqrt{(I_{\rm lim})^2 - \left(|I''_{q1}| + |I''_{q2}|\right)^2}\right) \\ I''_{d2} = 0 \end{cases} \tag{8}$$

where $K_{1,2}$ are the control gains in sequence loops. $P_{\rm in}$ is the pre-fault DC power, assumed constant during faults.

Substituting (7)–(8) into (6), it yields,

$$\dot{\boldsymbol{I}}_1 = \dot{\boldsymbol{I}}_{\rm source} - Y_1 \cdot \dot{\boldsymbol{V}}_1, \ \dot{\boldsymbol{I}}_2 = Y_2 \cdot \dot{\boldsymbol{V}}_2 \tag{9}$$

where $\dot{\boldsymbol{I}}_{\rm source} = (I''_{d1} - j \cdot K_1/M)\exp(j \cdot \angle\dot{\boldsymbol{V}}_1)$, $Y_1 = K_1/(j \cdot M)$ and $Y_2 = j \cdot K_2/M$ are the current source, the positive and negative sequence admittances. Eq. (9) follows with the fault sequence models in Fig. 3.

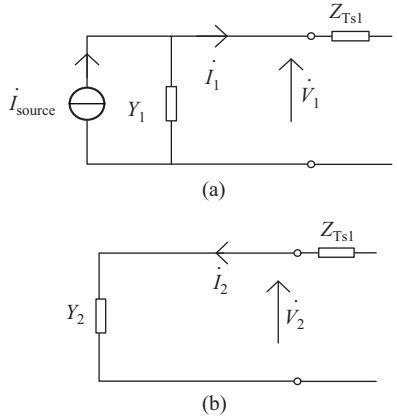

Fig. 3. Fault model of GSC. (a) Positive sequence. (b) Negative sequence.

Based on the above GSC fault model, we can see:

1) The high voltage side fault current $\dot{\boldsymbol{I}}_{\rm s}$ is fully determined by the low voltage side WP current $\dot{\boldsymbol{I}}$.

2) Type-4 WPs behaves as a controlled current source, and the sequence impedances, relating to the control parameters in the respective sequence circuits, are different.

3) The positive sequence control of the type-4 WP has a nonlinear characteristic, and the superposition theorem is not applicable, i.e. the current distribution factor D_1 is no longer valid for the 'active' positive sequence electric network.

In short, the existing Z-1-TLT scheme is not suitable for the system condition connecting WPs.

III. Improved Tilting Scheme of Reactance Element in Distance Protection

In this section, an improved Z-1-TLT scheme is developed by incorporating the fault behavior of GSC control. The basic principle is also to estimate the angle θ_{AMI}. By tilting the reactance element at a similar angle during resistive faults, the relay over-reach (or under-reach) can be compensated actively. The difficulty is $\dot{\boldsymbol{I}}_{\mathrm{r}}$ being an unavailable electrical quantity for the local relay device, which is resolved in this section.

A. Tilting Angle Estimation

Take the fault AG, for example. (1) is revised as,

$$Z_{\mathrm{app}}^{\mathrm{AG}} = mZ_1 + \frac{\dot{\boldsymbol{I}}_{\mathrm{f}}}{\dot{\boldsymbol{I}}_{\mathrm{sa}} + k_0\dot{\boldsymbol{I}}_{\mathrm{s0}}} R_{\mathrm{f}} \tag{10}$$

where $\dot{\boldsymbol{I}}_{\mathrm{sa}}$ is the faulty phase current. Furthermore, the fault current at fault point meets $3\dot{\boldsymbol{I}}_{\mathrm{f1,2,0}} = \dot{\boldsymbol{I}}_{\mathrm{f}}$.

According to the fault model of GSC in Fig. 3(b), we can infer the negative sequence network of Fig. 1 is passive. This also applies to the zero-sequence network. Thus, we can determine the corresponding current distribution factors.

$$\dot{\boldsymbol{I}}_{\mathrm{s2}} = \dot{\boldsymbol{I}}_{\mathrm{f2}} D_2, D_2 = \frac{(1-m)Z_1 + Z_{\mathrm{r1}}}{1/Y_2 + Z_{\mathrm{Ts1}} + Z_1 + Z_{\mathrm{r1}}} \tag{11}$$

$$\dot{\boldsymbol{I}}_{\mathrm{s0}} = \dot{\boldsymbol{I}}_{\mathrm{f0}} D_0, D_0 = \frac{(1-m)Z_0 + Z_{\mathrm{r0}}}{Z_{\mathrm{Ts0}} + Z_0 + Z_{\mathrm{r0}}} \tag{12}$$

Subsequently, the unknown fault current $\dot{\boldsymbol{I}}_{\mathrm{f}}$ can be eliminated along with the sequence currents at the relay location based on the current distribution relationships in negative and zero sequence systems, referring to [14]. (10) can be then revised as,

$$Z_{\mathrm{app}}^{\mathrm{AG}} = mZ_1 + \frac{3R_{\mathrm{f}}}{\left(\frac{\dot{\boldsymbol{I}}_{\mathrm{s1}}+\dot{\boldsymbol{I}}_{\mathrm{s2}}}{\dot{\boldsymbol{I}}_{\mathrm{s0}}} + (1+k_0)\right) D_0} \tag{13}$$

For other two typical asymmetrical faults, i.e. faults BC and BCG, the simplified apparent impedance are directly given as,

$$Z_{\mathrm{app}}^{\mathrm{BC}} = mZ_1 + \frac{R_{\mathrm{f}}}{\left(1 - \frac{\dot{\boldsymbol{I}}_{\mathrm{s1}}}{\dot{\boldsymbol{I}}_{\mathrm{s2}}}\right) D_2} \tag{14}$$

$$Z_{\mathrm{app}}^{\mathrm{BCG}} = mZ_1 + \frac{\frac{2}{D_2} + \frac{\dot{\boldsymbol{I}}_{\mathrm{s0}}}{\dot{\boldsymbol{I}}_{\mathrm{s2}} D_0}}{\left(1 - \frac{\dot{\boldsymbol{I}}_{\mathrm{s1}}}{\dot{\boldsymbol{I}}_{\mathrm{s2}}}\right)} R_{\mathrm{f}} \tag{15}$$

From (13)–(15), the tilting angle θ_{AMI} can be calculated,

$$\theta_{\mathrm{AMI}} = \begin{cases} -\angle\left(\frac{\dot{\boldsymbol{I}}_{\mathrm{s1}}+\dot{\boldsymbol{I}}_{\mathrm{s2}}}{\dot{\boldsymbol{I}}_{\mathrm{s0}}} + 1 + k_0\right) D_0 \\ -\angle\left(1 - \frac{\dot{\boldsymbol{I}}_{\mathrm{s1}}}{\dot{\boldsymbol{I}}_{\mathrm{s2}}}\right) D_2 \\ \angle\left(\frac{2}{D_2} + \frac{\dot{\boldsymbol{I}}_{\mathrm{s0}}}{\dot{\boldsymbol{I}}_{\mathrm{s2}} D_0}\right) / \left(1 - \frac{\dot{\boldsymbol{I}}_{\mathrm{s1}}}{\dot{\boldsymbol{I}}_{\mathrm{s2}}}\right) \end{cases} \tag{16}$$

A concern is that parameter m used in the current distribution factors (D_0, D_2) is unknown. To resolve this, we can utilize the following assumptions:

1) Distance protection detects the internal (or external) faults rather than estimates the accurate fault position;

2) Only the apparent impedance tilt, caused by remote faults approaching the protective boundary, can compromise the relay function's security.

Thus, a constant m representing zone 1 length is selected to maintain high accuracy of θ_{AMI} for marginal faults. For other fault positions, the faults can also be detected correctly due to relay redundancy. This is analyzed later in this paper.

Table I compares the used electrical quantities of both the existing and improved tilting angle estimation methods, we can see the improved method mainly omits the requirements of two-side electromotive forces and the transmission angle.

TABLE I
Comparison of The Used Electrical Quantities

Existing Z-1-TLT scheme	Improved Z-1-TLT scheme
• Line sequence impedance • Source impedance at both sides • Two-side electromotive forces and transmission angle	• Line sequence impedance • Source impedance at remote side; Negative/zero sequence impedance at WP side system

B. Pickup Condition of Reactance Element Tilt Setting

In the above section, the estimation of θ_{AMI} for three typical asymmetrical grid faults and the parameter selection principle has been elaborated. However, the reactance element does not need to tilt for all faults in a practical application. Because only specific fault positions can lead to malfunction of the relay using a standard, horizontal reactance element setting.

In this section, the malfunction risk area of the relay device under different impedance tilt conditions is analyzed. To define the pickup condition for the proposed reactance element tilt setting, another tilt angle of apparent impedance relative to the set-point on the line is defined as,

$$\theta_{\mathrm{ref}} = \angle\left(Z_{\mathrm{app}} - Z_{\mathrm{set}}\right) \tag{17}$$

where Z_{set} is the line impedance from relay to zone 1 set-point.

Take the condition of clockwise impedance tilt, for example. Distance relay security is compromised by external faults approaching the protective boundary. Under such conditions, Fig. 4(a) depicts the malfunction risk area of the distance relay on the complex plane. Red line represents the line impedance. Assuming the counter-clockwise direction is positive. From the relative relationship between θ_{ref} and θ_{AMI}, we can build the following pickup condition for the malfunction risk area marked in Fig. 4(a),

$$\theta_{\mathrm{AMI}} \le \theta_{\mathrm{ref}} < 0 \tag{18}$$

If the pickup condition (18) is satisfied, the reactance element needs to tilt at an angle θ_{AMI} actively in the clockwise

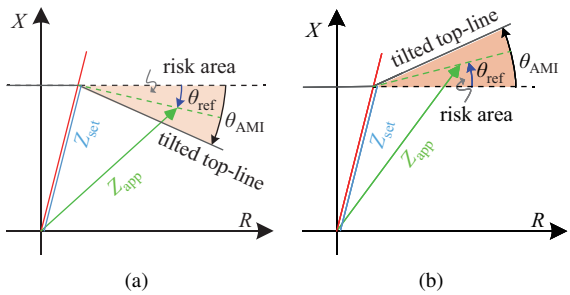

Fig. 4. Malfunction risk area under different impedance tilt conditions. (a) Clockwise impedance tilt. (b) Counter-clockwise impedance tilt.

direction. For other impedance locations out of the risk area, the horizontal reactance setting is capable of dealing with the fault.

On the contrary, internal faults towards the protective boundary may threaten the correct operation of distance relay under the counter-clockwise impedance tilt condition. Fig. 4(b) shows the corresponding complex plane representation for the malfunction risk area of distance relay under such condition. Based on the relative relationship between θ_{ref} and θ_{AMI}, the corresponding pickup condition is built as,

$$\theta_{\text{AMI}} \geq \theta_{\text{ref}} > 0 \tag{19}$$

Similarly, under counter-clockwise impedance tilt conditions, the reactance element needs to tilt an angle θ_{AMI} in the counter-clockwise direction only if pickup condition (19) is satisfied.

Combining the malfunction risk area detection in (18) and (19), the implementation procedure of the improved Z-1-TLT scheme is illustrated in the flowchart of Fig. 5.

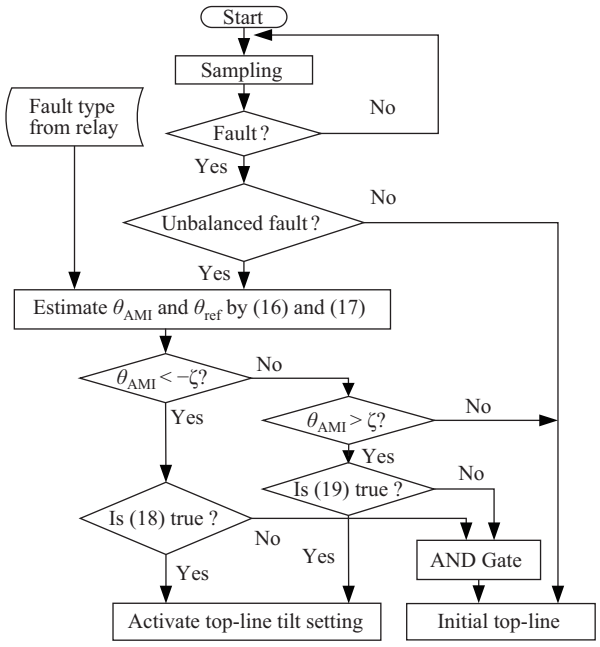

Fig. 5. Flowchart of the improved Z-1-TLT scheme.

The angle θ_{AMI}, in fact, can indicate the direction of apparent impedance tilt, which is adopted for the selection of pickup conditions. ζ is a positive minimum to avoid the jitter of the impedance tilt directional detection. When θ_{AMI} is within $[-\zeta, \zeta]$, it means the measured reactance approximates its accurate value.

In detail, the implementation procedure consists of five steps:

1) Fault detection in the start unit and fault phase selector.

2) If symmetrical faults occur, jump to step 5). Otherwise, start the angle estimation for both θ_{AMI} and θ_{ref}.

3) Judge the impedance tilting direction, if $\theta_{\text{AMI}} \in [-\zeta, \zeta]$, jump to 5). Otherwise, judge the pickup condition (18) or (19).

4) If one of the pickup conditions is satisfied, tilt the zone 1 top-line by an angle θ_{AMI}.

5) Otherwise, maintain the initial zone 1 top-line setting.

IV. Simulation Verification

To verify the effectiveness of the improved Z-1-TLT scheme, a 110 kV WP outgoing system is modeled in DIgSILENT/PowerFactory, as shown in Fig. 6. The WP has a rated power of 200 MW and the system operates at 50 Hz. In this paper, zone 1 length is set covering 80% of L1, while zone 2 reaches 50% of the next segment. The second segment includes two paths, i.e. L21 and L22, to simulate the meshed external conditions. Three lines are all 40 km. Sequence impedance parameters of the transmission line (in per km), the transformer, and the remote source are the same as in [14].

A. Fault Condition of Clockwise Impedance Tilt

Technically, relay DR in the test system is at high risk of over-reach if the WP still delivers a large amount of active power during grid faults. In this subsection, the improved Z-1-TLT scheme is verified under such fault conditions possibly causing relay over-reach. At this moment, the GSC active current control follows (6). Control parameters are listed in Table II.

TABLE II
Parameters of GSC Controller During Grid Faults

Category	K_1	K_2	$I_{q\text{lim}}$	I_{lim}	P_{in}
Value (p.u.)	2.5	2	1	1.2	1

As the discussion on (18) in Section II-B, mainly external faults threaten the relay's selectivity. Table III compares the tilting angles θ_{AMI} and θ_{ref} during different Zone 2 (boundary) faults of Fig. 6. Real value of the estimated θ_{AMI}, i.e. θ^*_{AMI}, is also included. In the table, the dotted-box marked scenarios dissatisfy the pickup condition (18), meaning the initial top-line setting is effective for the detection of these external faults. For other scenarios, angle θ_{ref} are negative, i.e. DR

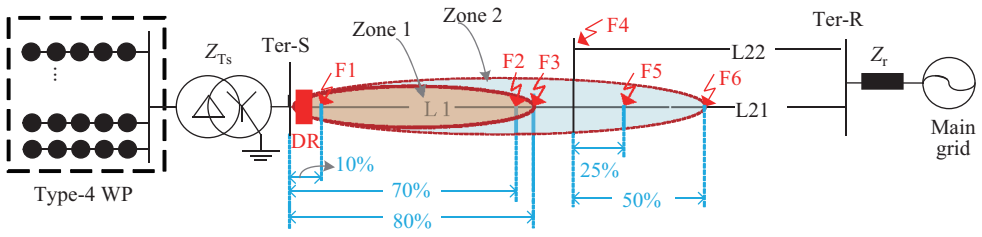

Fig. 6. Type-4 WP outgoing test system.

TABLE III
COMPARISON OF DIFFERENT EXTERNAL (BOUNDARY) FAULTS

Fault type	Condition R_f	F3 θ_{ref}	F3 θ_{AMI}	F3 θ^*_{AMI}	F4 θ_{ref}	F4 θ_{AMI}	F4 θ^*_{AMI}
AG	5	−10.8	−10.8	−10.8	1.7	−12.8	−13.2
	10	−10.0	−10.0	−10.0	−4.1	−12.0	−12.4
	50	−11.0	−11.0	−11.0	−10.1	−12.9	−13.2
BC	5	−30.2	−30.2	−30.2	−21.9	−28.1	−28.9
	10	−16.7	−16.7	−16.7	−10.7	−14.3	−15.1
	50	−14.2	−14.2	−14.2	−13.7	−15.3	−16.0
BCG	5	−28.4	−28.4	−28.4	−20.2	−26.4	−27.2
	10	−12.9	−12.9	−12.9	−7.7	−11.2	−12.0
	50	−12.6	−12.6	−12.6	−12.4	−13.8	−14.6
		F5			F6		
AG	5	16.7	−17.4	−6.9	18.6	−20.6	−9.4
	10	3.6	−16.1	−11.4	4.5	−18.8	−14.4
	50	−9.3	−15.2	−15.7	−9.5	−16.6	−18.6
BC	5	−2.2	−29.1	−16.2	4.8	−28.2	−13.9
	10	−5.5	−20.5	−14.8	−4.7	−23.7	−18.1
	50	−12.9	−17.3	−17.9	−12.7	−18.0	−20.2
BCG	5	−1.3	−28.0	−15.2	5.7	−26.8	−12.8
	10	−3.6	−18.2	−12.8	−3.2	−21.6	−16.4
	50	−11.9	−15.8	−16.8	−11.9	−16.5	−19.2

Note: θ^*_{AMI} represents the real value of θ_{AMI}.

always 'sees' internal faults under the initial top-line condition. Meanwhile, θ_{AMI} and θ_{ref} meet the pickup condition (18), indicating DR 'sees' external faults if the top-line tilts θ_{AMI}.

1) Zone 2 Faults on Local Line

First, we consider external faults on the local line, i.e. located at F4. Take the fault AG located at F4 ($R_f = 10\,\Omega$), for example. Fig. 7(a) shows the instantaneous currents at the WP side, the current references of the DSC system, and the sequence voltages at the PCC point. The dynamic angles in Fig. 7(b) show that θ_{AMI} and θ_{ref} converge to their steady states after a short transient fluctuation. As shown in Fig. 7(c), DR is at risk of malfunction under the initial top-line setting, i.e. over-reach. However, the problem can be avoided if the revised top-line setting is adopted.

Compared with Fig. 7, Fig. 8 depicts the same fault at F4, but a high fault resistance ($R_f = 500\,\Omega$) is considered. Clearly, the improved Z-1-TLT scheme is unaffected by high fault resistance. After adopting the revised top-line setting, DR will correctly 'see' the tested external fault. Note that, to cover the high resistive faults, a large 'resistance' setting, i.e. the right boundary of polygonal zone, needs to be initialized, as shown in Fig. 8(b). This should be configured in advance, which is no longer discussed in this section.

2) Boundary Faults

The compensating accuracy of the improved Z-1-TLT scheme for boundary faults determines the selectivity of the distance relay. This can be seen from the fault scenarios located at F3 in Table III, where DR 'sees' boundary faults as $\theta_{AMI} = \theta_{ref}$. Moreover, the dynamic results of fault BC located at F3 ($R_f = 10\,\Omega$) are given. In Fig. 9(a), the pickup condition (18) is satisfied rapidly. In Fig. 9(b), the apparent impedance is located below the initial top-line setting but on the revised zone 1 top-line. Thus, the boundary fault can be detected correctly.

3) Zone 2 Faults on Downstream Line

In view of the relaying reliability, apart from the reliable

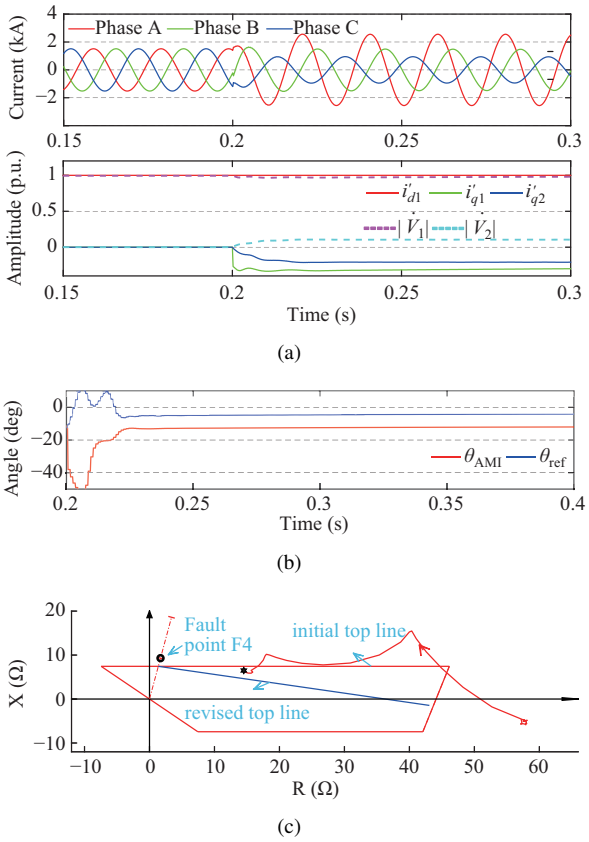

Fig. 7. Fault AG at point F4 ($R_f = 10\,\Omega$). (a) Fault currents and control signals; (b) Dynamic angles θ_{AMI} and θ_{ref}; (c) Trajectory of Z^{AG}_{app}.

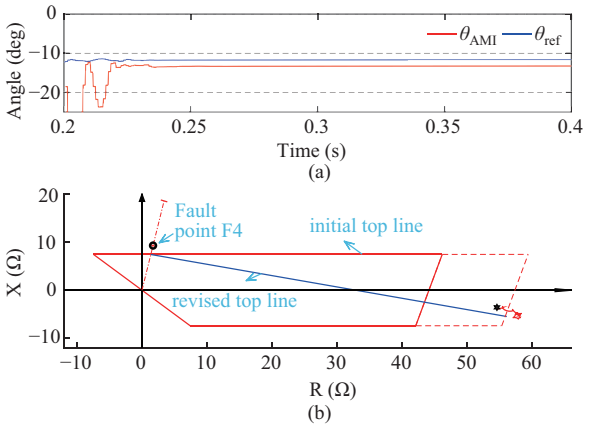

Fig. 8. Fault AG at point F4 ($R_f = 500\,\Omega$). (a) Dynamic angles θ_{AMI} and θ_{ref}. (b) Trajectory of Z^{AG}_{app}.

action for the faults on the local line, zone 1 element should not act for zone 2 faults on downstream line. Due to the meshed configuration in transmission level, it is meaningful to consider the effect of intermediate infeed, i.e. the path L22 in Fig. 6.

Take the zone 2 fault on the line L21 in Fig. 10, for example. The measured impedance of (1) should be revised as,

$$Z_{app} = Z_{L1} + \frac{\dot{\boldsymbol{I}}_s + \dot{\boldsymbol{I}}_i}{\dot{\boldsymbol{I}}_s} Z_{fL21} + \Delta Z = Z_{L1} + Z_{fL21} + \Delta Z_i + \Delta Z \quad (20)$$

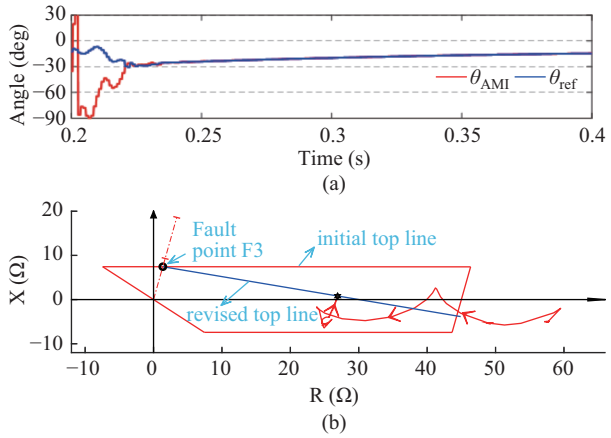

Fig. 9. Fault BC at point F3 ($R_{\rm f} = 10\,\Omega$). (a) Dynamic angles $\theta_{\rm AMI}$ and $\theta_{\rm ref}$. (b) Trajectory of $Z_{\rm app}^{\rm BC}$.

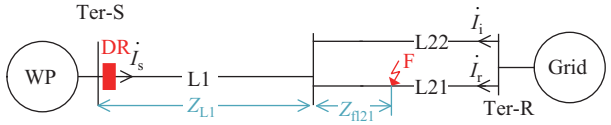

Fig. 10. Single-line fault diagram of WP outgoing system for the fault on L21.

where $Z_{\rm L1}$ is the line impedance of L1. $Z_{\rm fL21}$ is the impedance of intermediate connection point to fault point of line L21. $\dot{\boldsymbol{I}}_i$ is the in-feed current on L22. Note, $\Delta Z = R_{\rm f}(\dot{\boldsymbol{I}}_i + \dot{\boldsymbol{I}}_{\rm r} + \dot{\boldsymbol{I}}_{\rm s})/\dot{\boldsymbol{I}}_{\rm s}$.

Compared with (1), a 'virtual' impedance ΔZ_i related to the in-feed current $\dot{\boldsymbol{I}}_i$ is introduced. The real tilting angle $\theta_{\rm AMI}^*$ will be $\angle(\Delta Z + \Delta Z_i)$, causing the deviation of $\theta_{\rm AMI}$ to $\theta_{\rm AMI}^*$. Here, we analyze this angular deviation from two aspects.

For a fault, if $R_{\rm f}$ is ignorable, ΔZ_i is dominated, i.e. $\theta_{\rm AMI}^* \approx \angle\Delta Z_i$. Consider the same source property of $\dot{\boldsymbol{I}}_i$ and $\dot{\boldsymbol{I}}_{\rm r}$, we know,

$$\begin{aligned}\angle\Delta Z_i &= \angle\left(\dot{\boldsymbol{I}}_i/\dot{\boldsymbol{I}}_{\rm s}\right) + \angle Z_1 \gg \angle\left(\dot{\boldsymbol{I}}_i/\dot{\boldsymbol{I}}_{\rm s}\right)\\ &\approx \angle\left(\left(\dot{\boldsymbol{I}}_i + \dot{\boldsymbol{I}}_{\rm r}\right)/\dot{\boldsymbol{I}}_{\rm s}\right)\end{aligned} \tag{21}$$

Generally, grid strength being sufficiently large compared to WP, $\dot{\boldsymbol{I}}_{\rm s}$ is much smaller than $\dot{\boldsymbol{I}}_i + \dot{\boldsymbol{I}}_{\rm r}$ in magnitude. Thus, we can infer $\angle\left(\left(\dot{\boldsymbol{I}}_i + \dot{\boldsymbol{I}}_{\rm r}\right)/\dot{\boldsymbol{I}}_{\rm s}\right) \approx \angle\left(\left(\dot{\boldsymbol{I}}_i + \dot{\boldsymbol{I}}_{\rm r} + \dot{\boldsymbol{I}}_{\rm s}\right)/\dot{\boldsymbol{I}}_{\rm s}\right)$, i.e. $\theta_{\rm AMI}^* \gg \theta_{\rm AMI}$.

As mentioned in [13], in the presence of WP, the angular difference of $\dot{\boldsymbol{I}}_i$ to $\dot{\boldsymbol{I}}_{\rm s}$, relating to the WP control, is uncertain. This does not affect to the above angular deviation analysis.

From another aspect, if $R_{\rm f}$ is very large, ΔZ is dominated, i.e. $\theta_{\rm AMI}^* \approx \angle\Delta Z$. Under such fault conditions, the intermediate infeed has an ignorable effect on the deviation of $\theta_{\rm AMI}$ to $\theta_{\rm AMI}^*$.

From the test scenarios in the columns of F5 and F6 in Table III, we can see the deviation of $\theta_{\rm AMI}$ to $\theta_{\rm AMI}^*$ for different faults all agree with the above angular deviation analysis with different $R_{\rm f}$. Specific to the evident angular deviation (i.e. $\theta_{\rm AMI}^* \gg \theta_{\rm AMI}$) during ignorable $R_{\rm f}$ scenarios, the clockwise impedance tilt is actually overcompensated, which does not affect the zone 2 fault detection on downstream line.

In summary, the improved Z-1-TLT scheme is effective to compensate for the influence of relay over-reach, in the fault conditions of clockwise impedance tilt.

B. Fault Condition of Counter-clockwise Impedance Tilt

In contrast to the fault conditions discussed in Section IV-A, if very little (or even no) active power is generated from the WP during grid faults, DR probably 'sees' the counter-clockwise impedance tilt, i.e. relay under-reach. In this subsection, the effectiveness of the improved zone tilting scheme under such fault conditions is verified. To simulate such fault conditions, GSC active current control is no longer as (6) but with an extra active current limiter in the positive sequence control loop. Other control parameters are the same as in Table II.

As the discussion on equation (19), the malfunction risk area under the fault conditions of counter-clockwise impedance tilt covers the internal fault points approaching the protective boundary and the boundary one. Table IV compares the tilting angles $\theta_{\rm AMI}$ and $\theta_{\rm ref}$ during different internal faults of Fig. 6. In the simulation, the active current limiter, i.e. $I_{d1\rm lim} = 0.2$ p.u., is activated after the faults occur at 0.2 s. In the table, the dotted-box marked scenarios dissatisfy the pickup condition (19), meaning the initial top-line setting is effective for the detection of these internal faults. For other scenarios, angle $\theta_{\rm ref}$ are positive, i.e. DR always 'sees' external faults under the initial top-line condition. Meanwhile, $\theta_{\rm AMI}$ and $\theta_{\rm ref}$ meet the pickup condition (19), indicating DR 'sees' internal faults if the top-line tilts $\theta_{\rm AMI}$.

TABLE IV
ANGULAR COMPARISONS DURING DIFFERENT ZONE 1 FAULTS

Fault Condition		F1			F2		
type	$R_{\rm f}$	$\theta_{\rm ref}$	$\theta_{\rm AMI}$	$\theta_{\rm AMI}^*$	$\theta_{\rm ref}$	$\theta_{\rm AMI}$	$\theta_{\rm AMI}^*$
AG	5	−69.6	1.5	2.2	−8.6	1.1	1.2
	10	−46.2	2.7	3.3	−2.6	2.0	2.2
	40	−10.6	3.0	3.6	2.3	3.4	3.6
BC	5	−35.5	−2.1	−1.0	0.3	3.6	3.9
	10	−12.6	5.7	6.8	7.2	8.9	9.1
	25	5.2	12.7	13.8	7.1	7.8	8.0
BCG	5	−26.6	10.4	10.8	−4.6	−0.9	−0.7
	10	2.8	21.6	21.9	7.9	9.8	10.0
	40	7.8	12.4	12.9	2.0	2.4	2.6

Take the fault AG located at F2 ($R_{\rm f} = 40\,\Omega$), for example. The dynamic results are displayed in Fig. 11. As displayed in Fig. 11(a), the activation of an active current limiter results in clearly reduced fault current contributions. In Fig. 11(b), $\theta_{\rm AMI}$ and $\theta_{\rm ref}$ rapidly converge to their steady states after the transient fluctuation, satisfying the pickup condition (19). Furthermore, in Fig. 11(c), an external fault is detected under the initial top-line setting, but a boundary fault is 'seen' when the revised zone 1 top-line is adopted.

Above results prove the improved Z-1-TLT scheme is also effective to compensate for the influence of relay under- reach, in the fault conditions of counter-clockwise impedance tilt.

C. Influence Analysis of Varying System Conditions

The influences of varying system conditions on the improved Z-1-TLT scheme are further analyzed in this section.

1) Different Capacities of the WP

As shown in Fig. 12, three different initial capacities (pre-fault) of the local WP, i.e. 50 MW, 100 MW, and 200 MW, are compared for a remote fault AG located at F4. (Take the fault condition of clockwise impedance tilt, for example).

From Fig. 12(a), we see that steady-state θ_{ref} increases with decrease of WP capacity. Comparing the three capacity conditions, it is positive only when the WP capacity is 50 MW, meaning the pickup condition (18) is no longer satisfied under such capacity conditions, in other words, the initial top-line setting is capable of detecting the fault. As the impedance trajectory in Fig. 12(b), an external fault is detected under the capacity condition of 50 MW. For another two capacity conditions, the revised top-line settings can compensate for the influence of impedance tilts, respectively. From this test case, we see the variation of the initial capacity condition of the local WP does not affect performance of the improved Z-1-TLT scheme.

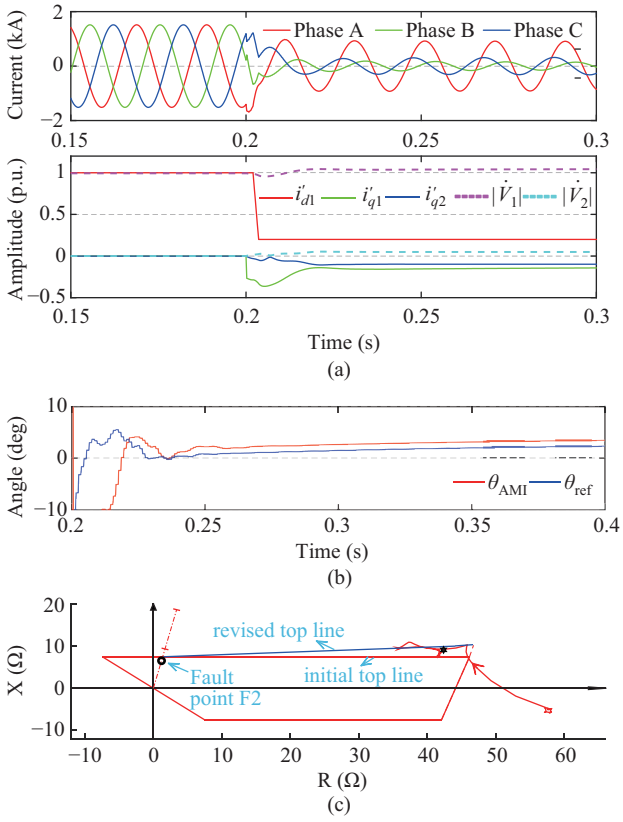

Fig. 11. Fault AG at F2 ($R_{\text{f}} = 40\,\Omega$). (a) Fault currents and control signals. (b) Dynamic angles θ_{AMI} and θ_{ref}. (c) Trajectory of $Z_{\text{app}}^{\text{AG}}$.

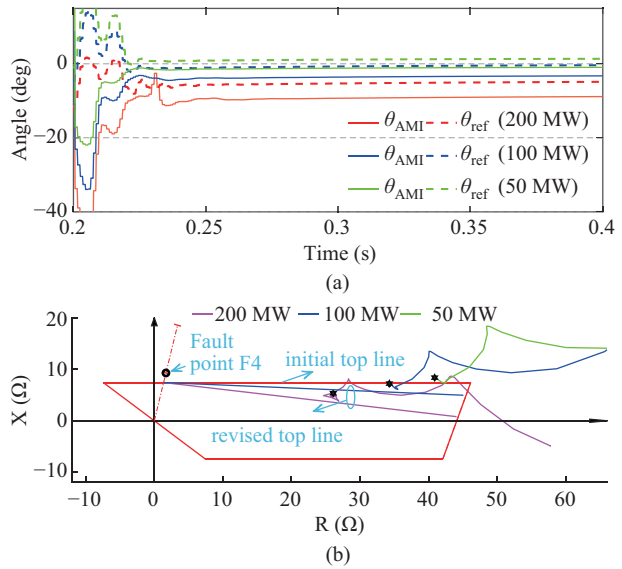

Fig. 12. Fault AG at point F4 ($R_{\text{f}} = 25\,\Omega$), under different WP capacities. (a) Dynamic angles θ_{AMI} and θ_{ref}. (b) Trajectories of $Z_{\text{app}}^{\text{AG}}$.

2) Flexible Operation of the WP

In contrast to the varying pre-fault capacity of the local WP in the above test, here we consider the varying capacity of WP during faults. It is possible, since the WP may run in varying conditions after faults due to the under-voltage (or overcurrent) generator protective limits. Assume that a certain percentage of generating units in the WP are tripped due to faults.

An external fault AG ($R_{\text{f}} = 25\,\Omega$) located at F4 under the fault condition of clockwise impedance tilt is tested. Here, take 50% of the generating units tripping at 0.3 s, for example. From Fig. 13(a), we can see the evident variations of the WP current due to the generating units tripping. From Fig. 13(b), we see the pickup condition (18) has been satisfied stably before 0.3 s. Correspondingly, an external fault is correctly detected when adopting the revised top-line (dashed blue) setting, see the apparent impedance location (square marked) in the impedance plane of Fig. 13(c). After the tripping action at 0.3 s, we see the pickup condition (18) is also satisfied stably, although the steady-state angles θ_{AMI} and θ_{ref} are

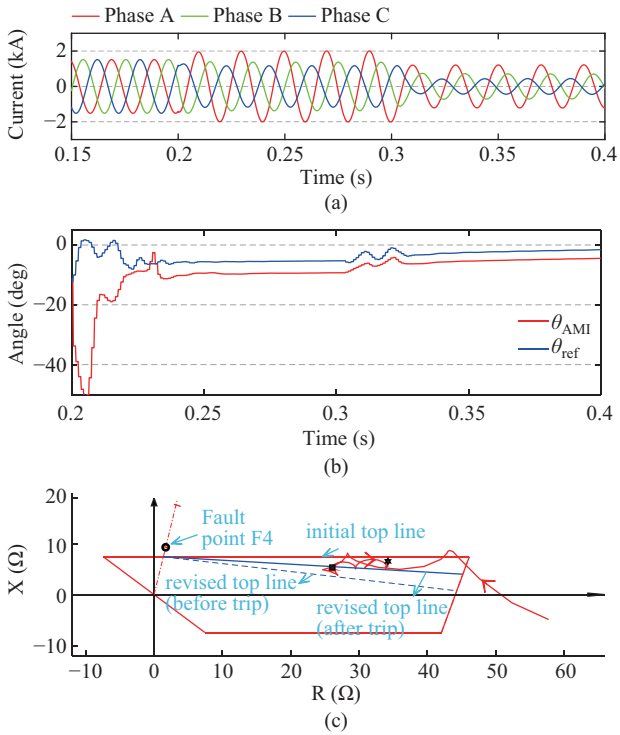

Fig. 13. Fault AG at F4 ($R_{\text{f}} = 25\,\Omega$), in the case of varying WP fault operation. (a) Fault currents. (b) Dynamic angles θ_{AMI} and θ_{ref}. (c) Trajectory of $Z_{\text{app}}^{\text{AG}}$.

slightly different. Under such conditions, the external fault is also correctly detected when adopting the revised top-line (solid blue), see the apparent impedance location (hexagram marked) in Fig. 13(c). This proves the improved Z-1-TLT scheme is immune to the flexible operation of the WP.

Generally, the WP behaves intermittently generating features due to fluctuation of wind speed. The influence on the new Z-1-TLT scheme is similar the above varying capacity but much slighter. The above influence of the varying WP capacity can be seen as a step disturbance. However, the turbine response is much slower than fluctuation of wind speed. Besides, the protection system usually concerns the fault condition within dozens to hundreds of milliseconds. Within this time interval, the turbine response to the fluctuation of wind speed tends to ramp up (or down) most.

3) Balanced Current Control

Except for the above DSC deployment, balanced current control (BCC) is another typical regulation method for type-4 WPs, regulating positive sequence current only, regardless of fault types. Under such control deployment, the adaptability of the improved Z-1-TLT scheme for different asymmetrical faults, and the countermeasures are discussed in Appendix A.

In this subsection, a fault BC ($R_{\rm f} = 10\,\Omega$) located at F3 is tested to verify the countermeasures in Appendix A. Fig. 14 illustrates the results, in the presence of BCC scheme deployed in WP system. As shown in Fig. 14(a), the WP outputs the balanced current only during the unbalanced fault. In Fig. 14(b), the angles $\theta_{\rm AMI}$ and $\theta_{\rm ref}$ fulfill the pickup condition (18) rapidly. At the same time, we see this boundary fault can be correctly detected, as the apparent impedance finally locates on the revised top line finally in Fig. 14(c).

4) System Operating Voltage and External Grid Configuration

Furthermore, the improved Z-1-TLT scheme is assessed based on a 220 kV test system, which considers a different system configuration. As shown in Fig. B1, the test system is modeled in RTDS, detailed system parameters are listed in Fig. B1 (b). In this scenario, the setting of zones 1 and 2 are the same as in Fig. 6.

Figure B2 corresponds to one external fault AG (located at the remote ends of both local line and zone 2) in case of clockwise impedance tilt conditions. From Fig. B2 (a), we can see the pickup condition (18) is satisfied, rapidly. Besides, the apparent impedance locates within zone 1 under the initial top-line setting, see the impedance plane representation of $Z_{\rm app}^{\rm AG}$ in Fig. B2 (b). However, an external fault will be detected in case of the revised top-line setting.

Moreover, an internal fault BC, approaching the zone 1 end, is also tested and results are given in Fig. B3. Clearly, the angular results in Fig. B3 (a) rapidly meet the pickup conditions (19), corresponding to the counter-clockwise impedance tilt conditions. In Fig. B3 (b), is different to the detected external fault under initial top-line setting, the internal fault is correctly detected in the case of the revised top-line setting.

The above tests prove the improved Z-1-TLT scheme is unaffected by the variations of system operating voltage and configuration of the external grid. So does the influence of different fault inception angles. This has been proven by the fault scenarios in Fig. B2 and B3, which respectively occur at 0.159 s and 0.224 s, i.e. having different fault inception angles.

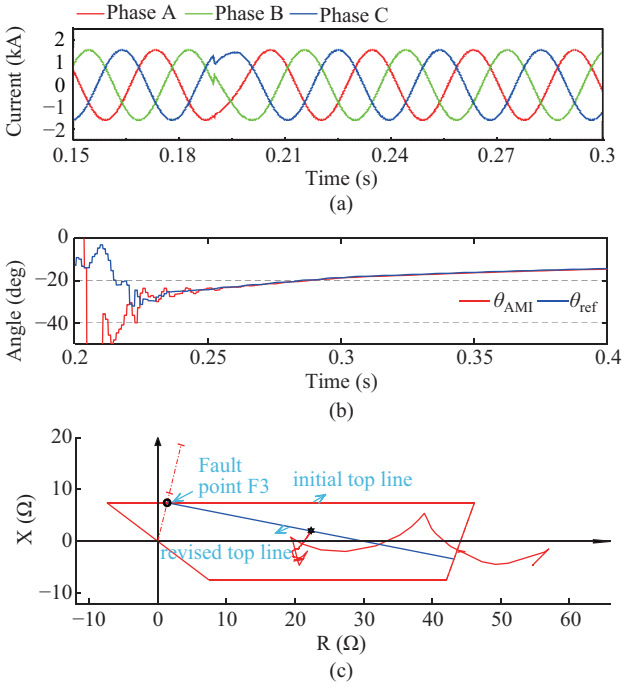

Fig. 14. Fault BC at point F3 ($R_{\rm f} = 10\,\Omega$), in the case of BCC deployment. (a) Fault currents. (b) Dynamic angles $\theta_{\rm AMI}$ and $\theta_{\rm ref}$. (c) Trajectory of $Z_{\rm app}^{\rm BC}$.

D. Error Analysis of Constant m Initialization

In the improved Z-1-TLT scheme, zone 1 length $m_{[0]}$ is used to initialize the current distribution factors $D_{0,2}$. It guarantees high accuracy of $\theta_{\rm AMI}$ for boundary faults, since $m_{[0]}$ coincides with the real fault distance. See the angular results in Table III and IV, where estimated $\theta_{\rm AMI}$ equals its real value $\theta_{\rm AMI}^{*}$ only for boundary fault scenarios in column F3. However, there are certain estimating errors in $\theta_{\rm AMI}$ for other fault positions due to the angular errors of $D_{0,2}|_{m=m_{[0]}}$.

1) Consideration of Network Property

The derivation of improved Z-1-TLT scheme is based on a general situation of the transmission grids connecting WP, and do not include any special network property assumption.

In [16]–[18], it is reported the homogeneity in a transmission network makes the equivalent grid impedance proportional to the line impedance for each sequence component, i.e. $Z_{\rm r1,2,0} = k_{c1,2,0}Z_{1,2,0}$, where $k_{c1,2,0}$ are real-valued coefficients. Under such conditions, the angles of $D_{2,0}$ are more simple in form.

$$\angle D_2 = \angle\frac{(1-m)Z_1 + Z_{\rm r1}}{1/Y_2 + Z_{\rm Ts1} + Z_1 + Z_{\rm r1}} = \angle\frac{Z_1}{1/Y_2 + Z_{\rm Ts1} + Z_1 + Z_{\rm r1}} \tag{22}$$

$$\angle D_0 = \angle\frac{(1-m)Z_0 + Z_{\rm r0}}{Z_{\rm Ts0} + Z_0 + Z_{\rm r0}} = \angle\frac{Z_0}{Z_{\rm Ts0} + Z_0 + Z_{\rm r0}} \tag{23}$$

From (22) and (23), we know the tilting angle $\theta_{\rm AMI}$ in (16)

is unaffected by the fault distance m. The above analysis indicates the source impedance angle, i.e. $\angle Z_{\rm r}$, can affect the error property of $\theta_{\rm AMI}$, evidently. Thus, accounting for different source impedance angles in the error analysis is necessary.

2) Constant m Initialization with Zone 1 Length

Drawing on the qualitative analysis method of this parameter selection mentioned in [14], at the fault steady-state, the tilt angle $\theta_{\rm AMI}$ for fault AG in (16) can be revised as,

$$\theta_{\rm AMI} = -\angle\left[\left(\frac{\dot{\boldsymbol{I}}_{\rm s1}+\dot{\boldsymbol{I}}_{\rm s2}}{\dot{\boldsymbol{I}}_{\rm s0}}+1+k_0\right)D_0\Big|_{m=\text{real fault dis.}}\right]+\delta_{D_0} \tag{24}$$

where δ_{D_0} is the propagated error from the $m=m_{[0]}$ selection, meeting $\delta_{D_0}=\left(\theta^*_{D_0}-\theta_{D_0}\right)$. θ_{D_0} and $\theta^*_{D_0}$ correspond to the angle of D_0 based on the constant parameter $m_{[0]}$ and the real per unit fault distance, respectively.

Figure 15 shows the variation of angular error δ_{D_0} against the varying fault distance from Ter-S to the zone 2 end. In the figure, different source impedance angles are compared. When fault distance increases, δ_{D_0} shows a monotonic property, and it is zero at zone 1 set point. The monotonic directions are different under different conditions of $\angle Z_{\rm r}$. The one of $\angle Z_{\rm r}=79.7^\circ$ corresponds to the homogeneous network condition discussed in the above subsection D-1).

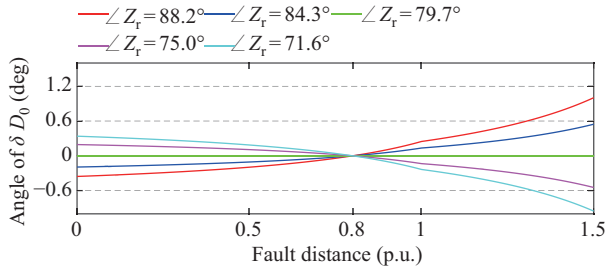

Fig. 15. Angular variation of D_0 against different fault positions.

From Fig. 15, Table V further concludes the error property of $\theta_{\rm AMI}$. Take the column of $\angle Z_{\rm r}=88.2^\circ$ being larger than the line impedance angle, for example. The test scenarios of fault AG in previous, e.g. the columns F3 and F4 in Table III, as well as those in Table IV, accord with the error property of $\theta_{\rm AMI}$ listed in this column.

TABLE V
ERROR PROPERTY OF $\theta_{\rm AMI}$ UNDER DIFFERENT SOURCE IMPEDANCE

$\angle Z_{\rm r}$	88.2°	84.3°	79.7°	75.0°	71.6°
$m<m_{[0]}$	$\theta_{\rm AMI}<\theta^*_{\rm AMI}$		$\theta_{\rm AMI}=\theta^*_{\rm AMI}$	$\theta_{\rm AMI}>\theta^*_{\rm AMI}$	
$m=m_{[0]}$	$\theta_{\rm AMI}=\theta^*_{\rm AMI}$		$\theta_{\rm AMI}=\theta^*_{\rm AMI}$	$\theta_{\rm AMI}=\theta^*_{\rm AMI}$	
$m>m_{[0]}$	$\theta_{\rm AMI}>\theta^*_{\rm AMI}$		$\theta_{\rm AMI}=\theta^*_{\rm AMI}$	$\theta_{\rm AMI}<\theta^*_{\rm AMI}$	

Note,
1. Source impedance magnitudes are $|Z_{\rm r1}|=3.1436$ and $|Z_{\rm r0}|=4.7154$.
2. Column 88.2° corresponds to the source impedance condition in previous tests, while the line impedance angle is around $\angle 79.7^\circ$.

The above error property also applies to the current distribution factor D_2, in the case of constant-valued parameter initialization, if the corresponding propagated error is similarly defined as $\delta_{D_2}=\left(\theta^*_{D_2}-\theta_{D_2}\right)$. This is similarly proven by the test scenarios of fault BC in columns F3 and F4 of Table III, as well as those in Table IV. Apart from the angular condition of $\angle Z_{\rm r}=88.2^\circ$, another two angular conditions, i.e. 79.7° and 71.6°, are tested, see Table VI. The dotted-box marked scenarios dissatisfy the pickup conditions (19), meaning DR can detect these internal faults under the initial top-line setting. For other scenarios, DR always faces risk of malfunction under the initial top-line condition. However, DR will operate correctly if the top-line tilts at $\theta_{\rm AMI}$. Besides, the table results meet the corresponding error property in Table V, see columns $\angle Z_{\rm r}=79.7^\circ$ and $\angle Z_{\rm r}=71.6^\circ$.

TABLE VI
ANGULAR COMPARISONS FOR FAULT BC UNDER DIFFERENT $\angle Z_{\rm r}$ CONDITION

Fault Condition			F1			F2		
	$\angle Z_{\rm r}$	$R_{\rm f}$	$\theta_{\rm ref}$	$\theta_{\rm AMI}$	$\theta^*_{\rm AMI}$	$\theta_{\rm ref}$	$\theta_{\rm AMI}$	$\theta^*_{\rm AMI}$
under-reach	79.7°	5	−34.5	0.25	0.25	−0.8	2.9	2.9
		20	4.5	15.2	15.2	11.2	12.2	12.2
	71.6°	5	−33.7	2.4	1.4	0.9	4.9	4.6
		20	5.3	17.1	16.0	12.6	13.9	13.6
			F3			F4		
over-reach	79.7°	5	−28.2	−28.2	−28.2	−19.4	−26.3	−26.4
		20	−12.2	−12.2	−12.2	−11.2	−14.3	−14.3
	71.6°	5	−26.3	−26.3	−26.3	−17.0	−24.7	−24.1
		20	−11.4	−11.4	−11.4	−10.2	−13.9	−13.3

In summary, we can clarify the influence from three aspects, 1) When $\angle Z_{\rm r}$ equals the line impedance angle, i.e. having homogeneity in the transmission network, $\theta_{\rm AMI}$ has high estimating accuracy for any faults along the protected line.

2) When $\angle Z_{\rm r}$ is smaller than line impedance angle, the error property of $\theta_{\rm AMI}$ enlarges the relative angle of $\theta_{\rm AMI}$ to $\theta_{\rm ref}$ for both internal and external faults, which brings in the positive influence on the reliability of the improved Z-1-TLT scheme.

3) When $\angle Z_{\rm r}$ is larger than line impedance angle, the error property of $\theta_{\rm AMI}$ will narrow the relative angle of $\theta_{\rm AMI}$ to $\theta_{\rm ref}$ for both internal and external faults, which has a slightly negative influence on the improved Z-1-TLT scheme, but do not affect relay selectivity. This is because the estimating error of $\theta_{\rm AMI}$ will be in a tiny range in the normal transmission network practice due to the not extremely large difference of X/R ratios between the equivalent source and the line. Take the largest angular condition $\angle Z_{\rm r}=88.2^\circ$ in Fig. 15, for example. The maximum δ_{D_0} is around 1°. The X/R ratio of the source impedance at this moment (around 31.8) is much larger than the typical range of 3–5 at the tested 110 kV voltage level [22].

E. Bolted Faults

During resistive grid faults, the above tests prove the improved Z-1-TLT scheme can improve reliability of distance protection. However, relay only 'sees' the line impedance during bolted grid faults on the local line, as the modulating impedance tends to zero at this moment. Besides, the angle $\theta_{\rm ref}$ in the pickup conditions (18) and (19) may be unstable for bolted faults approaching the protective boundary. Thus, the initial top-line setting is suggested in a selected dead zone, where the measured resistance is smaller than a pre-defined

threshold. In this paper, a simple resistance-based dead zone detection method is introduced. In detail,

$$\Delta R = \text{real}\,(Z_{\text{app}}) - \frac{\text{imaginary}\,(Z_{\text{app}})}{\text{imaginary}\,(Z_1)}\text{real}\,(Z_1) < R_{\text{thr}} \quad (25)$$

where R_{thr} is the threshold of the dead zone detection.

In Fig. 16, the fault AG at point F3 (under the condition of clockwise impedance tilt) is taken as an example to elaborate the sensitivity of the introduced dead zone detection. In the figure, the variable ΔR under several small fault resistance cases is plotted, where the steady-state ΔR increases clearly with the increase of fault resistance. This proves feasibility of the above dead zone detection method.

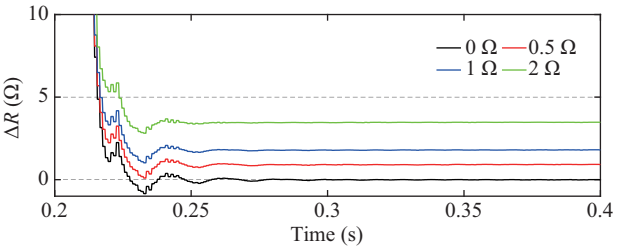

Fig. 16. ΔR variation for fault AG located at F3 when R_{f} increases.

In the flowchart of Fig. 5, an additional step is needed after step 2): Run dead zone detection. If the criterion (25) is satisfied, jump to step 5). Otherwise, go into step 3) as before.

V. Discussion

Distance protection in the outgoing line of a WP has malfunction risks due to the apparent impedance tilt feature during resistive grid faults. An improved Z-1-TLT scheme with the combination of the GSC fault control is proposed in this paper, which can be integrated into the existing polygonal distance relays as a special function for its application in the outgoing systems of type-4 WPs (or photovoltaic plants). The properties of the improved Z-1-TLT scheme are concluded as:

1) The improved scheme compensates for the unexpected reactance measurement error by tilting the zone 1 top-line at an estimated angle to avoid relay overreach or under-reach.

2) According to the malfunction risk area division and dead zone detection, the improved scheme only activates in risk areas, improving protective efficiency and reliability.

3) The improved Z-1-TLT scheme needs the coordination of time delay functions, e.g. one power frequency cycle, to avoid transient instabilities and uncertainties.

4) This paper focuses on functional improvement of the impedance element. Start unit, phase selector, and other elements are assumed to work properly.

5) To estimate the tilting angle, the impedance parameters of the remote grid in the reduced 'two-machine' system is needed, keeping the same as the existing Z-1-TLT scheme in [22]. Alternatively, the grid impedance estimating methods in [24], [25] based on only the PCC voltage and current measurements can also guarantee the feasibility of the improved Z-1-TLT scheme.

6) In this paper, three typical unsymmetrical grid faults, e.g. fault AG, fault BC, and fault BCG, are used to verify the effectiveness of the improved Z-1-TLT scheme. It should be mentioned the formulation of θ_{AMI} for other asymmetrical faults can be obtained with relevant fault boundary conditions.

Current distribution factors in the negative or (and) zero sequence systems is (are) used to eliminate the unknown remote current in-feed. The improved Z-1-TLT scheme has application limits. In detail, it cannot apply to symmetrical grid faults, as the negative-sequence fault loop stays in the open-circuit condition at the WP side. Nor, does it apply to the grounded faults in the non-grounded medium (or low) voltage system (zero-sequence circuit in such system is absent).

VI. Conclusion

Aiming at the malfunction risk of distance protection in the WP outgoing system, an improved Z-1-TLT scheme is developed to enhance the relaying reliability in this paper. In principle, modern digital distance relay allows the tilting of the top-line in the protective zone, which enables feasibility of the improved Z-1-TLT scheme. Besides, the improved Z-1-TLT scheme only employs local fault information, which benefits from the steady-state fault modeling analysis of the WP. To improve operating efficiency and reliability of the new Z-1-TLT scheme, the auxiliary criteria for malfunction risk area and dead zone are built for collaborative decisions. Simulation results reveal the feasibility of the new Z-1-TLT scheme and its effectiveness against different influences, including changes in system conditions, fault conditions, WP operations, etc. Comparative assessment with conventional protection shows the strength of the proposed method.

Appendix A

For the deployment of BCC scheme in the WP system, the improved Z-1-TLT scheme is effective to L-G faults only. Under such condition, we can revise the tilting angle in (17) by eliminating the WP's negative sequence current (i.e. $\dot{\boldsymbol{I}}_{\text{s2}} = 0$),

$$\theta_{\text{AMI}}^{\text{AG}} = -\angle\left(\frac{\dot{\boldsymbol{I}}_{\text{s1}}}{\dot{\boldsymbol{I}}_{\text{s0}}} + (1+k_0)\right) D_0 \quad \text{(A1)}$$

For interphase (ground) faults, the new Z-1-TLT scheme has application limits due to the invalid factor D_2. However, we can revise the expressions of θ_{AMI} in (17) for fault BC and BCG based on the estimations for the fault current $\dot{\boldsymbol{I}}_{\text{f}}$ in [17], [18].

$$\theta_{\text{AMI}}^{\text{BC}} = \angle\frac{\dot{\boldsymbol{I}}_{\text{fbc}}}{\dot{\boldsymbol{I}}_{\text{sbc}}} = \angle\frac{\dot{\boldsymbol{I}}_{\text{f1}} - \dot{\boldsymbol{I}}_{\text{f2}}}{\dot{\boldsymbol{I}}_{\text{s1}} - \dot{\boldsymbol{I}}_{\text{s2}}} = \angle\frac{\dot{\boldsymbol{U}}_{\text{f2}} \approx \dot{\boldsymbol{U}}_{\text{s2}}}{\dot{\boldsymbol{I}}_{\text{s1}}(Z_{\text{r1}} + (1-m)Z_1)} \quad \text{(A2)}$$

$$\theta_{\text{AMI}}^{\text{BCG}} = \angle\frac{\dot{\boldsymbol{I}}_{\text{fb}} + \dot{\boldsymbol{I}}_{\text{fc}}}{\dot{\boldsymbol{I}}_{\text{sb}} + \dot{\boldsymbol{I}}_{\text{sc}} + 2k_0\dot{\boldsymbol{I}}_{\text{s0}}} = \angle\frac{3\dot{\boldsymbol{I}}_{\text{f0}}}{\dot{\boldsymbol{I}}_{\text{s0}}(2+2k_0) - \dot{\boldsymbol{I}}_{\text{s1}}}$$
$$= -\angle\left((2+2k_0) - \frac{\dot{\boldsymbol{I}}_{\text{s1}}}{\dot{\boldsymbol{I}}_{\text{s0}}}\right) D_0 \quad \text{(A3)}$$

APPENDIX B

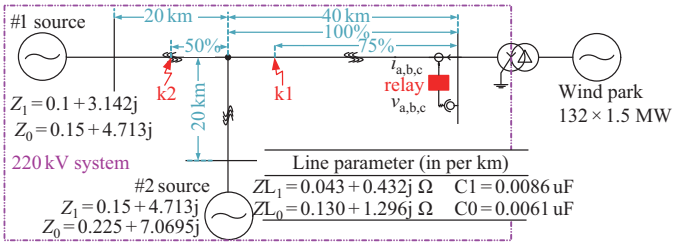

Fig. B1. Test system with intermediate infeed in real-time digital simulator (RTDS) (Note, to avoid confusion, fault points are tagged as k1, k2 in this test model).

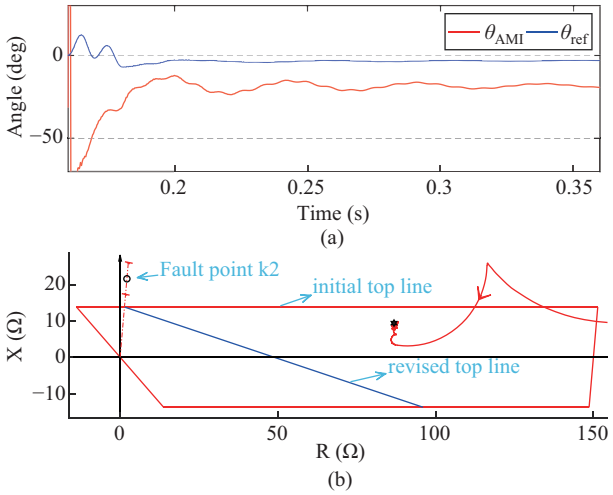

Fig. B2. Fault AG at point k2 ($R_f = 20\,\Omega$), occurring at 0.159 s. (a) Dynamic angles θ_{AMI} and θ_{ref}; (b) Trajectory of Z_{app}^{AG}.

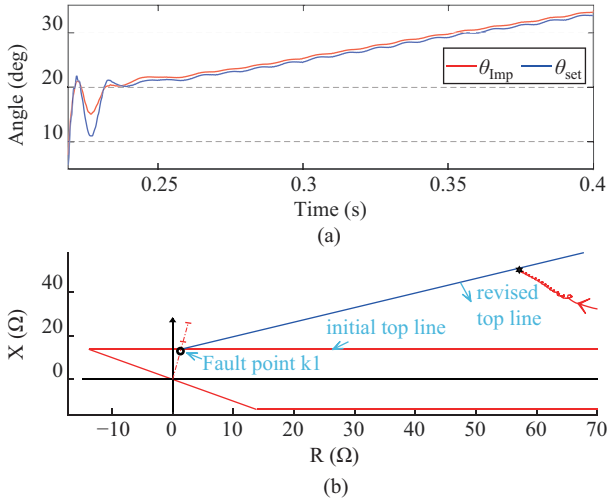

Fig. B3. Fault BC at point k1 ($R_f = 10\,\Omega$), occurring at 0.224 s. (a) Dynamic angles θ_{AMI} and θ_{ref}. (b) Trajectory of Z_{app}^{BC}.

REFERENCES

[1] P. Meibom, K. B. Hilger, H. Madsen, and D. Vinther, "Energy comes together in Denmark: the key to a future fossil-free Danish power system," *IEEE Power and Energy Magazine*, vol. 11, no. 5, pp. 46–55, Sep.-Oct. 2013.

[2] V. Telukunta, J. Pradhan, A. Agrawal, M. Singh, and S. G. Srivani, "Protection challenges under bulk penetration of renewable energy resources in power systems: a review," *CSEE Journal of Power and Energy Systems*, vol. 3, no. 4, pp. 365–379, Dec. 2017.

[3] D. Popovic and I. Wallace, "International review of fault ride through for conventional generators," KEMA, London, 16010829, Nov. 24, 2010.

[4] Y. Tsujii, T. Tsuji, T. Oyama, Y. Nakachi, and S. C. Verma, "A study on the frequency fluctuation in case of high penetration of renewable energy sources," *IEEJ Transactions on Power and Energy*, vol. 136, no. 1, pp. 33–43, Jan. 2016.

[5] F. Xiao, Y. J. Xia, K. Chen, K. P. Zhou, K. J. Zhang, and D. Yang, "Study on the influence of distance protection in power grid with new energy sources," in *Proceedings of the 2019 IEEE 3rd Conference on Energy Internet and Energy System Integration*, 2019, pp. 2568–2572.

[6] F. Gao, Z. Guan, S. Zhang, J. Zhang, and J. M. Dou, "Influence on transmission line relay protection under DFIG-based wind farm intergration," in *Proceedings of the 2015 5th International Conference on Electric Utility Deregulation and Restructuring and Power Technologies*, 2015, pp. 290–295.

[7] B. Li, J. Y. Liu, X. Wang, and L. L. Zhao, "Fault studies and distance protection of transmission lines connected to DFIG-based wind farms," *Applied Sciences*, vol. 8, no. 4, pp. 562, Apr. 2018.

[8] J. L. Suonan, Z. C. Wang, J. K. Zhang, X. H. Tong, L. Dai, and X. N. Kang, "A novel distance protection algorithm for high resistance grounding faults based on parameter identification," *Proceedings of the CSEE*, vol. 31, no. 31, pp. 173–178, Nov. 2011.

[9] Y. Fang, K. Jia, Z. Yang, Y. B. Li, and T. S. Bi, "Impact of inverter-interfaced renewable energy generators on distance protection and an improved scheme," *IEEE Transactions on Industrial Electronics*, vol. 66, no. 9, pp. 7078–7088, Sep. 2019.

[10] A. Hooshyar, M. A. Azzouz, and E. F. El-Saadany, "Distance protection of lines emanating from full-scale converter-interfaced renewable energy power plants—Part I: problem statement," *IEEE Transactions on Power Delivery*, vol. 30, no. 4, pp. 1770–1780, Aug. 2015.

[11] Y. L. Feng, Z. Zhang, Q. H. Lai, X. G. Yin, and H. Y. Liu, "Impact of inverter interfaced generators on distance protection," in *Proceedings of the 2019 4th International Conference on Intelligent Green Building and Smart Grid*, 2019, pp. 512–515.

[12] M. M. Sun, H. Wang, and X. R. Zhu, "Fault characteristics of photol-voltaic power station and its influence on relay protection of transmission line," in *Proceedings of the 5th IET International Conference on Renewable Power Generation*, 2016, pp. 1–5.

[13] A. Banaiemoqadam, A. Hooshyar, and M. A. Azzouz, "A control-based solution for distance protection of lines connected to converter-interfaced sources during asymmetrical Faults," *IEEE Transactions on Power Delivery*, vol. 35, no. 3, pp. 1455–1466, Jun. 2020.

[14] K. Q. Ma, Z. Chen, Z. Liu, C. L. Bak, and M. Castillo, "Protection collaborative fault control for power electronic-based power plants during unbalanced grid faults," *International Journal of Electrical Power & Energy Systems*, vol. 130, pp. 107009, Sep. 2021.

[15] A. K. Pradhan and G. Joos, "Adaptive distance relay setting for lines connecting wind farms," *IEEE Transactions on Energy Conversion*, vol. 22, no. 1, pp. 206–213, Mar. 2007.

[16] S. Paladhi and A. K. Pradhan, "Adaptive distance protection for lines connecting converter-interfaced renewable plants," *IEEE Journal of Emerging and Selected Topics in Power Electronics*, vol. 9, no. 6, pp. 7088–7098, Dec. 2021.

[17] Y. Y. Liang, W. L. Li, and Y. T. Huo, "Zone I distance relaying scheme of lines connected to MMC-HVDC stations during asymmetrical faults: problems, challenges, and solutions," *IEEE Transactions on Power Delivery*, vol. 36, no. 5, pp. 2929–2941, Oct. 2021.

[18] Y. Y. Liang, W. L. Li, and W. T. Zha, "Adaptive mho characteristic-based distance protection for lines emanating from photovoltaic power plants under unbalanced faults," *IEEE Systems Journal*, vol. 15, no. 3, pp. 3506–3516, Sep. 2021.

[19] "Technische regeln für den anschluss von kundenanlagen an das hochspannungsnetz und deren betrieb (TAR Hochspannung)," FNN-Richtlinie VDE-AR-N 4120, Nov. 2018. https://www.vde.com/de/fnn/arbeitsgebiete/tar/tar-hochspannung-vde-ar-n-4120

[20] T. Kauffmann, U. Karaagac, I. Kocar, S. Jensen, E. Farantatos, A. Haddadi, and J. Mahseredjian, "Short-circuit model for type-IV wind turbine generators with decoupled sequence control, " *IEEE Transactions on Power Delivery*, vol. 34, no. 5, pp. 1998–2007, Oct. 2019.

[21] S. Paladhi, Q. Hong and C. D. Booth, "Adaptive distance protection for multi-terminal lines connecting converter-interfaced renewable energy sources," 16th International Conference on Developments in Power System Protection (DPSP 2022), pp. 31–35, 2022.

[22] G. Ziegler, *Numerical Distance Protection*: *Principles and Applications*, 4th ed., Erlangen: Publicis, 2011.

[23] X. G. Liu, Z. Xu, and K. P. Wong, "Recent advancement on technical requirements for grid integration of wind power," *Journal of Modern Power Systems and Clean Energy*, vol. 1, no. 3, pp. 216–222, Dec. 2013.
[24] S. Cobreces, E. J. Bueno, D. Pizarro, F. J. Rodriguez, and F. Huerta, "Grid impedance monitoring system for distributed power generation electronic interfaces," *IEEE Transactions on Instrumentation and Measurement*, vol. 58, no. 9, pp. 3112–3121, Sep. 2009.
[25] A. Moallem, D. Yazdani, A. Bakhshai, and P. Jain, "Frequency domain identification of the utility grid parameters for distributed power generation systems," in *Proceedings of the 2011 Twenty-Sixth Annual IEEE Applied Power Electronics Conference and Exposition*, 2011, pp. 965–969.

Kaiqi Ma received a B.Eng. and M.Eng. degrees from Hohai University, China, in 2012 and 2015, in Control Engineering, respectively. He was Research Associate at Research & Development Center of State Grid Xuji Group Corporation, China. Since 2018, he has been a Ph.D. student at the Department of Energy, Aalborg University, Denmark. His research interest includes distributed generation, advanced control, and power system protection.

Hans Kristian Høidalen (M'05–SM'14) received an M.Sc. and Ph.D. degrees in Electrical Engineering from the Norwegian University of Science and Technology (NTNU), Trondheim, Norway, in 1990 and 1998, respectively. He is currently a Professor with the NTNU, with a special interest in power system transients, as well as electrical stress calculations and modeling. He is the developer of the preprocessor to EMTP-ATP called ATPDraw. His current focus is the transformer analysis and power system protection.

Zhe Chen (M'95–SM'98–F'19) received a B.Eng. and M.Sc. degrees from Northeast China Institute of Electric Power Engineering, Jilin, China, in 1982, 1986, respectively, and a Ph.D. degree from University of Durham, U.K., in 1997. He is currently a Full Professor with the Energy Department, Aalborg University, Denmark. His main current research interests are wind energy and modern power systems. He is also a Fellow of the Institution of Engineering and Technology (London, U.K.), and a Chartered Engineer in the U.K.

Claus Leth Bak (M'95–SM'98) received a B.Sc. degree in Electrical Power Engineering from the Engineering College, Århus, Denmark, and an M.Sc. degree in Electrical Power Engineering with specialization in high voltage engineering from the Department of Energy, Aalborg University, Denmark, in 1994. He is currently a Professor with the Department of Energy, Aalborg University. His main research areas include corona phenomena on overhead lines, power system transient simulations, and power system protection. He is a member of Cigré C4.502, Cigré SC C4, and the Danish Cigré National Committee.